CrossMark

MULTISCALE MODELING AND EXPERIMENT

Phase field modeling for grain growth in porous solids

K. Ahmed[1] · T. Allen[2,3] · A. El-Azab[1,4]

Abstract Concurrent evolution of grain size and porosity in solids is a technically important problem involving curvature-driven motion of grain boundaries and the pore motion by surface diffusion. A phase field approach comprising a system of Cahn–Hilliard and Allen–Cahn equations has been developed recently to tackle this problem. Through a formal asymptotic analysis, the current work demonstrates that the phase field model recovers the corresponding sharp-interface dynamics of the co-evolution of grain boundaries and pores; this analysis also fixes the model kinetic parameters in terms of real materials properties. As a case study, the model was used to investigate the effect of porosity on the kinetics of grain growth in CeO_2 in 3D. It is shown that the model captures the phenomenon of pore breakaway often observed in experiments. Pores on three- and four-grain junctions were found to move along with the migrating boundary, while edge pores (on the boundary between two grains) were found to easily separate from the boundary. The simulations showed that pore breakaway leads to abnormal grain growth. The simulations also showed that grain growth kinetics in CeO_2 changes from boundary controlled to pore controlled as the amount of porosity increases. The kinetic growth parameters such as the growth exponent and the rate constant (or equivalently the activation energy) were found to depend strongly on the precise amount and distribution of porosity, which reconciles the different experimental results reported for grain growth in CeO_2.

Introduction

Grain growth is a process by which the average grain size of a polycrystalline solid increases with time at sufficiently high temperature. During this process, large grains grow at the expense of small ones leading to a reduction of the total grain boundary area and a decrease in the interfacial free energy of the polycrystalline solid. Thermal, electromagnetic, optical, and mechanical properties of polycrystalline solids depend on their grain size distribution [1, 2]. In addition, the grain size affects the behavior of the polycrystalline solids under extreme conditions such as high-temperature particle irradiation [3–5]. As such, many theoretical, computational, and experimental investigations have been carried out to understand the process of grain growth in solid materials [1, 2, 6–18].

For grain growth in pure and fully dense solids, which is usually termed as *ideal grain growth*, the classical models by Burke and Turnbull [7], Mullins [8], and Hillert [9] demonstrate that grain boundary motion is a mean-curvature-driven motion [10], meaning that the grain boundary velocity is proportional to the mean curvature of the grain boundary. This gives rise to the well-known parabolic kinetics for the average grain size [1, 2, 6–9]. However, modeling the process of grain growth kinetics in porous solids is more complicated by the interaction between the

✉ K. Ahmed
  ahmedk@purdue.edu

A. El-Azab
  aelazab@purdue.edu

1   School of Nuclear Engineering, Purdue University,
    West Lafayette, IN 47907, USA

2   Department of Engineering Physics, University of
    Wisconsin-Madison, Madison, WI 53706, USA

3   Present Address: Idaho National Laboratory, Idaho Falls,
    ID 83415, USA

4   School of Materials Engineering, Purdue University,
    West Lafayette, IN 47907, USA

grain boundaries and pores in such materials [1, 6, 11–18]. Basically, the pores exert a drag force on the grain boundaries and hinder their motion, thereby retarding the grain growth process. This pore-induced retardation of grain growth is an example of the so-called *particle-inhibited grain growth* [1]. Furthermore, nearby pores can in some cases merge together (coalesce) as they move along grain boundaries, and thus they themselves contribute to reduction of the interfacial free energy in solids. The concurrent pore coalescence and grain growth is known to proceed during the final stage of sintering in porous solids [1, 6].

The first models to investigate the effect of pores on grain growth were proposed by Nichols [11], Brook [12], and Carpay [13]. These models assume the microstructure to be homogeneous. Therefore, they only considered an isolated pore on a grain boundary and assumed the deduced kinetics represents the average kinetics of the whole system. Moreover, these models assume nearly spherical pores that can only move along with the boundary as a rigid body without changing their shape. They also neglect pore coalescence that usually takes place simultaneously with grain growth. Such simplified models succeeded at least qualitatively in describing some aspects of the physics of the process that were observed experimentally [1]. Nonetheless, the quantitative results of these models did not agree well with the experimental data. This discrepancy was primarily attributed to the absence of the details of the pore and grain boundary geometries in these models and the unrealistic assumption of a rigid body motion of pores.

In order to alleviate the shortcomings of the above mean field models, spatiotemporal models were proposed to take into consideration the details of the geometry of the pore and the boundary, and hence capture the nature of the heterogeneous structure of the system [14–17]. Evans and co-workers [14, 15] and later Riedel and Svoboda [16, 17] formulated the sharp-interface description of the problem. These sharp-interface models gave new insights that could not be gained from the classical models. For instance, it has been demonstrated that the possibility of pore separation depends strongly on the pore configuration. An edge pore between two grains detach easily from a migrating boundary, while a pore on a three-grain junction (a triple-junction pore) or a pore on a four-grain junction usually move along with the junction [16, 17]. However, as it is well known for all sharp-interface models, the task of solving these models numerically is cumbersome [14–17]. In particular, applying the boundary conditions for general pore/grain configurations and the criterion of pore separation is complicated [14–17]. In fact, only 2D numerical simulations have been conducted since Evans and co-workers introduced their formulation [14, 15] nearly three decades ago. Only recently, Barrett et al. [19] presented the first 3D solution of coupled surface and grain boundary

motion. However, that study was limited to bi- and tri-crystals with applications only to thermal grooving and sintering of two unequal-sized particles. Large scale 3D simulations of grain growth in porous solids based on the sharp-interface model have not been attempted yet. With this in mind, the motivation for developing a phase field (diffuse-interface) model of the problem is obvious.

The current authors have recently introduced a novel phase field model for investigating grain growth in porous solids [6, 18]. The model consists of coupled Cahn–Hilliard and Allen–Cahn equations that represent the coupling between the curvature-driven motion of the grain boundary and the surface diffusion-driven motion of the pore. The phase field model relaxes all the assumptions in the classical homogeneous models and avoids the numerical complications of the sharp-interface models. While our previous investigations were limited to 2D simulations of the model, we present here 3D simulations of the model for the first time. Furthermore, we carry out a formal asymptotic analysis of the phase field model, which demonstrates that the diffuse-interface description of the problem reduces to its sharp-interface counterpart as the diffuse-interface thickness approaches zero. This analysis both proves the consistency of the diffuse-interface model and enables us to determine the model parameters from the sharp-interface counterpart.

For the sake of obtaining quantitative results that can be compared with experiments, we present here 3D simulations of grain growth in porous ceria. Ceria has been chosen for its wide usage in several industrial applications such as in catalysis, sensors, and fuel cell technologies [20, 21]. It is also known to be a good surrogate material for uranium dioxide, which is the main nuclear fuel. The 3D simulations capture the phenomenon of pore breakaway which was artificially suppressed in 2D simulations. The dependence of pore separation on the pore configuration as predicted by the sharp-interface models [14–17] is confirmed. Moreover, 3D simulations also show that pore breakaway could cause abnormal grain growth. In agreement with the 2D simulations, the 3D simulations show that the process of grain growth retards with increasing porosity. The growth kinetics changes from boundary-controlled kinetics to pore-controlled kinetics as the level of porosity increases. However, due to the pore breakaway phenomenon, the rate constant (or equivalently the activation energy) is sensitive to the precise amount and distribution of porosity in each growth regime. Therefore, a detailed description of the underlying microstructure is required for obtaining accurate grain growth rates in porous solids and explaining the discrepancies in experimental grain growth data in porous solids.

This paper is organized as follows. In "Theoretical models of grain growth in porous solids" section, we

briefly review the theoretical models of grain growth in porous solids, e.g., the classical, sharp-, and diffuse-interface models. The asymptotic matching between the diffuse-interface and sharp-interface is then presented in "Asymptotic analysis of the phase field model" section. The results are then introduced and discussed in "Results and discussion" section, which are followed by the concluding remarks in "Concluding remarks" section.

Theoretical models of grain growth in porous solids

Classical models of grain growth in porous solids

In the classical models by Nichols [11], Brook [12], and Carpay [13], the microstructure is assumed to be homogeneous. Hence, only one pore-boundary complex is used to represent the behavior of the whole system [1]. According to these models, there are two different scenarios for the interaction between the pore and the boundary. In one case, the migrating boundary could separate from the pore. In the other, the migrating boundary could drag the pore along with it. If the boundary separates from the pore, the boundary moves with its intrinsic velocity as in the pore-free case. However, the separated pore can be picked up by another moving boundary but such situation is ignored in the classical models. The condition for pore breakaway can be derived once the dominant mechanism for pore migration is identified [1]. Pores can migrate by surface diffusion, evaporation and condensation, or lattice (volume) diffusion. In this manuscript, we will limit our discussion to the case of pore migration by surface diffusion since it is expected to be the prevailing mechanism for pore migration in most solids [1, 18]. When pores migrate via surface diffusion and assuming nearly spherical pore shape, the condition for pore breakaway takes on the form [1, 12],

$$\left(\frac{D_s w \delta}{D_a r^3}\right) D_{sep}^2 - D_{sep} + \pi r = 0. \tag{1}$$

In the above, D_s is the surface diffusion coefficient, w is the thickness of the surface diffusion layer, δ is the grain boundary thickness, D_a is the diffusion coefficient for the atomic jumps across the grain boundary, r is the pore size, and D_{sep} is the grain size at which pore separation occurs.

If the pore moves along with the boundary, the velocity of the pore-boundary complex is given by [1]

$$v = F_b \frac{M_p M_b}{M_p + N_p M_b}. \tag{2}$$

Here, the subscript b denotes the boundary and p the pore; v is the velocity, M the mobility, and F is the driving force. N_p is the average number of pores per boundary. Two limiting cases can be identified from Eq. (2). When $M_p \gg N_p M_b$, the effective velocity of the pore-boundary complex reduces to $v = M_b F_b$, and hence, the effect of pores on the boundary velocity is negligible, a case which is commonly referred to as *boundary-controlled* grain growth. On the other hand, when $M_p \ll N_p M_b$, the velocity of the pore-boundary complex becomes $v = M_p F_b / N_p$, and hence, the boundary velocity is limited by the pore mobility. This case is referred to as *pore-controlled* grain growth. The velocity of the pore-boundary complex can also take on intermediate values between these two extremes.

For the boundary-controlled case, one should expect the same parabolic grain growth kinetics derived for the pore-free system [7, 8]. However, for the pore-controlled case, a few growth laws for the average grain size were derived [1, 18]. In general, the growth law is a power law that has the form

$$D^n(t) - D_0^n = k\,t, \tag{3}$$

where $D(t)$ is the average grain size at time t, D_0 is the average initial grain size, and k is the rate constant. The value of the growth exponent n is dictated by the prevailing mechanism for pore migration. For pore migration via surface diffusion, $n = 4$ [1, 18].

In all the relations stated above, it was assumed that the microstructure is homogeneous, the pores have nearly spherical shape, and the pore shape does not change during the interaction with the migrating boundary. These assumptions are unrealistic and hence limit the applicability of the classical models. This motivated the community to develop more advanced models that relax these assumptions. Both sharp- and diffuse-interface (phase field) models have been proposed [6, 14–18]. Such models are spatiotemporal models that are able to take into account the detailed geometries of the pore and the grain boundary and hence the heterogeneity of the microstructure.

Sharp-interface modeling of grain growth in porous solids

The sharp-interface description of the problem was formulated by Evans and co-workers [14, 15]. In that description, the grain boundary moves by mean curvature, while the pore migrates via surface diffusion. This can be mathematically expressed as follows:

$$v_b = -\gamma^{gb} M_b \kappa_b, \tag{4}$$

$$v_p = \frac{\gamma^s D_s w\, \upsilon_m}{RT} \nabla_s^2 \kappa_s. \tag{5}$$

In the above, v_b is the velocity of a grain boundary element, v_p is the velocity of a surface element of the pores,

γ^{gb} is the grain boundary energy, κ_{b} is the grain boundary curvature, γ_{s} is the pore (free) surface energy, M_{b}, D_{s}, and w have the same definitions as in Eqs. (1) and (2), υ_{m} is the molar volume, R is the universal gas constant and T is the absolute temperature, ∇_{s}^2 is the surface Laplacian (Laplace operator on the surface), and κ_{s} is the curvature of the pore (free) surface. The curvature is positive for convex surfaces and negative for concave surfaces. Equation (5) indicates that the surface diffusion is modeled here as a motion by the surface Laplacian of the curvature following the pioneering work of Mullins [22].

Since the local excess chemical potential at the pore (free) surface is proportional to its curvature, κ_{s} and $\nabla \kappa_{\text{s}}$ must be continuous at the pore tip. Moreover, the balance of forces at triple-junctions requires that the dihedral angle, θ, defined by $\theta = 2\cos^{-1}(\gamma^{\text{gb}}/2\gamma^{\text{s}})$ to be maintained. Equations (4) and (5) with the just mentioned boundary conditions at the pore tip can be solved numerically for any pore/boundary configuration.

Evans and co-workers only obtained a steady-state solution for an idealized (axisymmetric) 2D geometry of an edge pore (a pore on a two-grain junction) [14, 15]. Later, Riedel, and Svoboda extended the analysis to other higher-order pore configurations (e.g., pores on three- and four-grain junctions) and non-steady-state motion [16, 17]. However, only idealized 2D geometries of the pore and grains were considered, so that the boundary conditions can easily be applied. Nevertheless, the solution of these simplified configurations improved our understanding of the problem. It was demonstrated that the possibility of pore breakaway depends on the pore configuration. Edge pores can directly separate from a migrating boundary, while higher-order pores must transform to edge pores (partial separation) before complete separation. Moreover, it was also shown that the rate constant (or equivalently the activation energy) is a function of the pore fraction for both boundary- and pore-controlled kinetics. Therefore, quantitative analysis of grain growth in porous solids requires a detailed description of the amount and distribution of porosity.

As mentioned above, for three decades, only 2D simulations of the sharp-interface model were conducted. Barrett et al. [19] have recently presented the first 3D solution of coupled surface and grain boundary motion. However, they have only considered simple test cases to validate their finite-element algorithm and numerical scheme. Large scale 3D simulations of the sharp-interface model of grain growth are yet to be performed probably because of numerical difficulties. Therefore, the development of a phase field (diffuse-interface) description of the problem is highly desirable since it is well known that such models can handle complex microstructures in a straightforward manner [23–25]. This has motivated us to tackle

the problem using the phase field approach as explained below.

Diffuse-interface modeling of grain growth in porous solids

While phase field models for sintering [26, 27], ideal grain growth [28, 29], and the effect of solute segregation on the kinetics of grain growth exist in the literature [30, 31], a phase field model of the effect of porosity on grain growth was lacking. The current authors have recently introduced a phase field model for grain growth in porous solids [6, 18]. The model can be summarized as follows. A combination of conserved and non-conserved order parameters (phase fields) is used to fully represent the microstructure of a porous polycrystalline solid [6, 18]. The conserved field, $\rho(x, t)$, represents the fractional density of the solid, and it takes the value of 1 in the solid phase and 0 in the pore phase. In order to distinguish between different grains with different orientations in the solid phase, a set of non-conserved order parameters, η_α, are used, where $\alpha = 1, 2, \ldots, p$, with p being the total number of grains in the solid. $\eta_\alpha = 1$ in the α-th grain and 0 otherwise. The microstructure evolution is captured by tracking the evolution of the conserved and non-conserved order parameters [23–25].

The free energy of the heterogeneous system of pores and grains can be constructed by invoking the formulation of Cahn and Hilliard for the free energy of non-uniform media [32]. In that formulation, the total free energy of the system is expressed in terms of the order parameters and their gradients. The specific form used here is

$$F = \int_\Omega \left[f(\rho, \eta_1, \ldots, \eta_\alpha, \ldots, \eta_p) + \frac{\kappa_\rho}{2} |\nabla \rho|^2 + \frac{\kappa_\eta}{2} \sum_{\alpha=1}^{p} |\nabla \eta_\alpha|^2 \right] d^3x.$$

(6)

In the above expression, the first term represents the bulk free energy density. The two gradient terms account for the excess free energy due to pore (free) surfaces and grain boundaries, respectively. Using constant gradient coefficients is equivalent to the assumption of isotropic surface and grain boundary energies. The bulk free energy density used here is simply a positive-definite multi-well potential that represents the equilibrium phases [6, 27]. It has the form

$$f(\rho, \eta_1, \ldots, \eta_\alpha, \ldots, \eta_p) = B\rho^2(1-\rho)^2$$
$$+ C\left[\rho^2 + 6(1-\rho)\sum_{\alpha=1}^{p}\eta_\alpha^2 - 4(2-\rho)\sum_{\alpha=1}^{p}\eta_\alpha^3 + 3\left(\sum_{\alpha=1}^{p}\eta_\alpha^2\right)^2 \right].$$

(7)

This particular from has $(p + 1)$ minima that correspond to the pore phase and all grains in the solid phase. B, C, κ_ρ,

and κ_η are material constants related to surface and grain boundary energies. These relations can be derived from the equilibrium profiles of the order parameters across flat interfaces as in the pioneering work by Cahn and Hilliard [32]. The details of such derivation for our case were given before in [6]. Here we only summarize the final results for completeness:

$$\gamma^{gb} = \frac{2}{\sqrt{3}}\sqrt{C\kappa_\eta}, \tag{8}$$

$$\gamma^{s} = \frac{1}{6}\sqrt{2(\kappa_\rho + \kappa_\eta)(B + 7C)}, \tag{9}$$

$$\ell = \sqrt{\frac{4\kappa_\eta}{3C}}, \tag{10}$$

$$\frac{6C}{\kappa_\eta} = \frac{B+C}{\kappa_\rho}. \tag{11}$$

In the above, ℓ is the diffuse-interface width. Equation (11) arises as a constraint on the free energy parameters due to the fact that the conserved and non-conserved order parameters have similar equilibrium profiles across the pore (free) surface (see [6] for details).

The kinetic evolution equations for the order parameters can then be derived following the standard approach of irreversible thermodynamic [33]. Following that approach, the order parameters evolve in such a way that the free energy of the system decreases monotonically with a non-negative entropy production. However, depending on whether the order parameter is a conserved or non-conserved quantity, additional constraints may apply.

The conserved density field evolves according to a Cahn–Hilliard equation [34] in the form

$$\frac{\partial\rho}{\partial t} = \nabla\cdot\mathbf{M}\nabla\mu = \nabla\cdot\mathbf{M}\nabla\frac{\delta F}{\delta\rho}$$
$$= \nabla\cdot\mathbf{M}\nabla\left[\frac{\partial f(\rho,\eta_1,\ldots,\eta_\alpha,\ldots,\eta_p)}{\partial\rho} - \kappa_\rho\nabla^2\rho\right]. \tag{12}$$

In the above equation, μ is a non-classical (non-local) chemical potential, $\delta F/\delta\rho$ is the functional derivative of the free energy with respect to the density field, and $\mathbf{M}$ is the Cahn–Hilliard (chemical) mobility tensor. In general, Cahn–Hilliard equation can represent different diffusion mechanisms, e.g., bulk, grain boundary, and surface [6]. However, we limit our study here to surface diffusion. The expression for the Cahn–Hilliard mobility tensor $\mathbf{M}$ has the form

$$\mathbf{M} = M^s\rho^2(1-\rho)^2\mathbf{T}^s, \tag{13}$$

where M^s is a constant that is related to the surface diffusivity as will be shown via the asymptotic matching later, and $\mathbf{T}^s$ is a surface projection tensor, which guarantees that the surface diffusion is tangential to the surface [6, 35]. $\mathbf{T}^s$ has the form

$$\mathbf{T}^s = \mathbf{I} - \mathbf{n}_s\otimes\mathbf{n}_s, \tag{14}$$

with $\mathbf{I}$ being the identity tensor and $\otimes$ representing the dyadic product, and $\mathbf{n}_s$ the unit normal to the pore (free) surface. The latter is given by $\mathbf{n}_s = \nabla\rho/|\nabla\rho|$.

The non-conserved order parameters are governed by a set of Allen–Cahn equations [36]:

$$\frac{\partial\eta_\alpha}{\partial t} = -L\frac{\delta F}{\delta\eta_\alpha} = -L\left[\frac{\partial f(\rho,\eta_1,\ldots,\eta_\alpha,\ldots,\eta_p)}{\partial\eta_\alpha} - \kappa_\eta\nabla^2\eta_\alpha\right]$$
$$\forall\alpha, \quad \alpha = 1, 2,\ldots,p, \tag{15}$$

where L, the Allen–Cahn mobility, is a material property that is directly related to the grain boundary mobility as will be shown via the asymptotic matching in the next section. By using a constant Allen–Cahn mobility, we assume isotropic grain boundary mobility.

The resulting coupled Cahn–Hilliard and Allen–Cahn dynamical system is able to couple the curvature-driven motion of the grain boundary (Eq. 4) with the pore motion by surface diffusion (Eq. 5).This will be shown using formal asymptotic analysis in the next section. Therefore, solving the set of kinetic Eqs. (12) and (15) reveals the microstructure evolution in a porous polycrystalline solid, and hence, the kinetics of grain growth in such materials can be investigated.

Asymptotic analysis of the phase field model

A typical procedure for carrying out an asymptotic analysis of a phase field model is by expanding the fields in terms of a small parameter, often given the symbol ε, that is related to the diffuse-interface width [23, 24, 31, 35, 37–40]. Two different expansions are usually employed, e.g., outer and inner expansions. The outer expansion describes the fields far away from the interface (in the bulk phases), and the inner expansion describes the fields in the neighborhood of the interface. Matching the solutions of the outer and inner problems deduced from these expansions in the limit $\varepsilon \to 0$ gives rise to the sharp-interface limit of the phase field (diffuse-interface) model. The matching conditions were derived and summarized several times before [24, 37], so we will not repeat that here. However, we will explicitly mention any matching condition we use here when necessary.

There are two phase field models [39, 40] that are relatively close to the one presented here in the sense that they also couple motion by mean curvature to motion by surface diffusion (motion by the surface Laplacian of the mean curvature). In [39], a phase field model of simultaneous order/disorder transition and phase separation was proposed. In that model, it was shown via asymptotic analysis that the antiphase boundary (the boundary between two variants of the ordered phase) moves by mean curvature

flow while the interphase boundary (the boundary between the ordered and disordered phases) moves by surface diffusion provided that the curvature of antiphase boundary is small and the curvature of the interphase is large. While in principle the pore (free) surface can be considered as an interphase and the grain boundary as an antiphase, the condition on the curvatures is restrictive. A pore moves by surface diffusion and a grain boundary moves by mean curvature flow regardless of their sizes/curvatures. In [40], a phase field model for the electromigration of intergranular voids was introduced. Using formal asymptotic analyses, the authors derived two different sharp-interface limits depending on the scaling of Allen–Cahn mobility. In one limit, the grain boundary was stationary while the void surface moves by surface diffusion. In the other limit, the grain boundary moves by mean curvature flow while the void surface moves by an evolution law that combines surface diffusion and surface attachment limited kinetics. As was first proposed by Taylor and Cahn [10], the evolution law that combines surface diffusion and surface attachment limited kinetics is considered to represent the general curvature-driven motion form which motion by mean curvature flow and motion by surface diffusion arise as limiting cases. Nevertheless, the two limits mentioned above do not reduce to the sharp-interface limit we seek here. Therefore, we present a different scaling that gives rise to a third limit. In this limit, the grain boundary moves by mean curvature flow and the pore surface moves by surface diffusion in agreement with the sharp-interface model (Eqs. 4 and 5). Also note that in [40], the authors used a non-differentiable (non-smooth) obstacle potential, while here we use a differentiable (smooth) multi-well potential.

Let us recast our model equations in a form similar to the one usually used in the asymptotic analyses reported in [24, 35–40]. The free energy (Eq. 6) is then rewritten as

$$
F = \int_{\Omega} [f(\rho, \eta_1, \ldots, \eta_\alpha, \ldots, \eta_p) + \frac{q\varepsilon^2}{2}|\nabla\rho|^2 \\
+ \frac{\varepsilon^2}{2}\sum_{\alpha=1}^{p}|\nabla\eta_\alpha|^2]d^3x.
$$

(16)

Hence, $q = \kappa_\rho/\kappa_\eta$ is a constant and $\varepsilon = \sqrt{\kappa_\eta}$ is a small parameter proportional to the diffuse-interface width (see Eq. 10). Moreover, we define

$$
\mu = \frac{\delta F}{\delta\rho} = [\partial_\rho f(\rho, \eta_1, \eta_2, \ldots, \eta_\alpha) - q\varepsilon^2\nabla^2\rho],
$$

(17a)

$$
u_\alpha = \frac{\delta F}{\delta\eta_\alpha} = [\partial_{\eta_\alpha} f(\rho, \eta_1, \eta_2, \ldots, \eta_\alpha) - \varepsilon^2\nabla^2\eta_\alpha] \\
\forall\alpha, \quad \alpha = 1, 2, \ldots, p.
$$

(17b)

Here μ is a chemical potential and u_α is a generalized force that drives the evolution of the non-conserved order

parameter, η_α. Furthermore, we make the slow time transformation $t \to \varepsilon^2 t$ suitable for the slow curvature-driven motion [31, 39]. The dynamical system (Eqs. 12 and 15) can then be rewritten as

$$
\varepsilon^2\partial_t\rho = \nabla \cdot M(\rho)\nabla\mu.
$$

(18)

$$
\varepsilon^2\partial_t\eta_\alpha = -Lu_\alpha \quad \forall\alpha, \alpha = 1, 2, \ldots, p.
$$

(19)

In Cahn–Hilliard equation above, we dropped its tensorial representation of the mobility and assumed that it is just function of ρ for simplicity. The projection tensor does not change the sharp-interface limit as was shown in [35]. In fact, in agreement with [35], we will show here that Cahn–Hilliard equation describes surface diffusion regardless of the form of the mobility as long as the bulk phases are in equilibrium. However, the importance of the projection tensor for numerical implementation will be discussed later.

As depicted in Fig. 1 below, the order parameters behave differently in the vicinity of a grain boundary or a pore (free) surface. Hence, the complete asymptotic analysis consists of two steps to deduce the equation of motion for each interface as in [39, 40]. Here, we first deduce an equation of motion for the grain boundary and then its counterpart for the pore (free) surface. In both the cases, along $\partial\Omega$, the boundary conditions are $\mathbf{m} \cdot M\nabla\mu = \mathbf{m} \cdot \nabla\rho = \mathbf{m} \cdot \nabla\eta_\alpha = 0$ where $\mathbf{m}$ denotes the unit normal to $\partial\Omega$. Under these conditions, the system is closed and the mass of the system is prescribed by the initial conditions. The results of the asymptotic analysis would not be altered if an open system with Dirichlet-type boundary conditions is considered instead [31, 38].

Derivation of the equation of motion of a grain boundary

Over a volume containing a single grain boundary (see Fig. 1a), the free energy (Eq. 16) reduces to

$$
F = \int [f(\rho = 1, \eta_1, \eta_2) + \frac{\varepsilon^2}{2}\sum_{\alpha=1}^{2}|\nabla\eta_\alpha|^2]d^3x.
$$

(20)

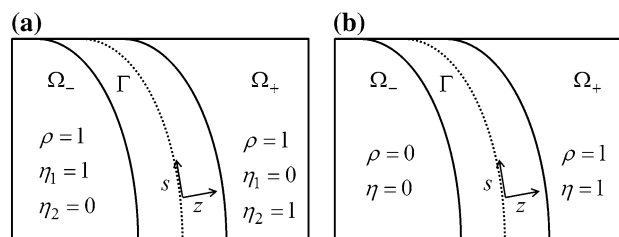The bulk free energy density (Eq. 7) is now given by

Fig. 1 A schematic illustration of the local coordinate system used in the asymptotic analysis showing values of the order parameters across **a** a grain boundary and **b** a free surface

$$f(\rho = 1, \eta_1, \eta_2) = C\left[1 - 4\left(\eta_1^3 + \eta_2^3\right) + 3\left(\eta_1^2 + \eta_2^2\right)^2\right].$$
(21)

In other words, the multi-well potential given by Eq. (7) reduces to a double well potential (Eq. 21) at a grain boundary.

Since the density is constant across a grain boundary, the dynamics is controlled by Allen–Cahn equations only. This is true as long as solute segregation is ignored. An asymptotic analysis for a phase field model of the effect of solute segregation on grain boundary motion was discussed in [31]. Hence, the dynamical system (Eqs. 18 and 19) reduces to

$$\varepsilon^2 \partial_t \eta_\alpha = -L u_\alpha \quad \forall \alpha, \quad \alpha = 1, 2$$
(22)

with the following initial and boundary conditions (see Fig. 1a):

$$\eta_1(x,0) = 1, \quad \eta_2(x,0) = 0 \quad \forall x \in \Omega_-,$$
(23a)

$$\eta_1(x,0) = 0, \quad \eta_2(x,0) = 1 \quad \forall x \in \Omega_+,$$
(23b)

$$\rho(x,0) = 1 \quad \forall x \in \Omega,$$
(23c)

$$\mathbf{m} \cdot \nabla \eta_1 = \mathbf{m} \cdot \nabla \eta_2 = 0 \quad \forall x \in \partial\Omega.$$
(23d)

In the outer region, we expand the fields as

$$u_\alpha(x,t) = u_\alpha^0(x,t) + \varepsilon u_\alpha^1(x,t) + \varepsilon^2 u_\alpha^2(x,t) + \cdots$$
$$\forall \alpha, \alpha = 1, 2,$$
(24)

with similar expressions for η_α. Note that superscripts on ε denote exponents, while superscripts on the fields u_α, η_α, μ, and ρ in the perturbation expansion. Explicit expressions of u_α^0, u_α^1, etc., can be obtained by expanding the derivatives of the bulk free energy (Eq. 21) in Taylor series as

$$\partial_{\eta_1} f(\eta_1, \eta_2) = \partial_{\eta_1} f(\eta_1^0, \eta_2^0) + \partial_{\eta_1}^2 f(\eta_1^0, \eta_2^0)[\varepsilon\eta_1^1 + \varepsilon^2\eta_1^2] + \partial_{\eta_2\eta_1}^2 f(\eta_1^0, \eta_2^0)[\varepsilon\eta_2^1 + \varepsilon^2\eta_2^2] + \cdots,$$
(25a)

$$\partial_{\eta_2} f(\eta_1, \eta_2) = \partial_{\eta_2} f(\eta_1^0, \eta_2^0) + \partial_{\eta_1\eta_2}^2 f(\eta_1^0, \eta_2^0)[\varepsilon\eta_1^1 + \varepsilon^2\eta_1^2] + \partial_{\eta_2}^2 f(\eta_1^0, \eta_2^0)[\varepsilon\eta_2^1 + \varepsilon^2\eta_2^2] + \cdots.$$
(25b)

By substituting Eqs. (25a and 25b) in (17b), and equating terms of the same order, we arrive at

$$u_1^0 = \partial_{\eta_1} f(\eta_1^0, \eta_2^0), \quad u_2^0 = \partial_{\eta_2} f(\eta_1^0, \eta_2^0),$$
(26a)

$$u_1^1 = \partial_{\eta_1}^2 f(\eta_1^0, \eta_2^0)\, \eta_1^1 + \partial_{\eta_2\eta_1}^2 f(\eta_1^0, \eta_2^0)\, \eta_2^1,$$
$$u_2^1 = \partial_{\eta_2}^2 f(\eta_1^0, \eta_2^0)\, \eta_2^1 + \partial_{\eta_1\eta_2}^2 f(\eta_1^0, \eta_2^0)\, \eta_1^1.$$
(26b)

We will need only explicit expressions for the fields up to first order in our analysis here. Substituting Eq. (26) in Eq. (22) and equating terms of the same order result in

different outer equations to be solved order by order. For the leading order (ε^0), we have

$$0 = -L u_\alpha^0 \quad \forall \alpha, \quad \alpha = 1, 2.$$
(27)

Taking into account the initial and boundary conditions, (Eqs. 23a–23d), Eq. 27 immediately gives,

$$u_\alpha^0 = 0 \quad \forall \alpha, \quad \alpha = 1, 2, \quad \forall x \in \Omega_\pm,$$
(28a)

$$\eta_1^0 = 1, \quad \eta_2^0 = 0, \quad \forall x \in \Omega_-,$$
(28b)

$$\eta_1^0 = 0, \quad \eta_2^0 = 1, \quad \forall x \in \Omega_-.$$
(28c)

For the next-to-the leading order (ε), we obtain

$$0 = -L u_\alpha^1 \quad \forall \alpha, \quad \alpha = 1, 2.$$
(29)

This immediately gives

$$u_\alpha^1 = 0 \quad \forall \alpha, \quad \alpha = 1, 2, \quad \forall x \in \Omega_\pm.$$
(30)

Now from the above expressions of u_α^1 and since by construction $\partial_{\eta_1\eta_2}^2 f(\eta_1^0, \eta_2^0) = \partial_{\eta_2\eta_1}^2 f(\eta_1^0, \eta_2^0) = 0$ and $\partial_{\eta_1}^2 f(\eta_1^0, \eta_2^0), \partial_{\eta_2}^2 f(\eta_1^0, \eta_2^0) > 0$ when the leading order outer solutions take on their equilibrium values (given by Eqs. 28b and 28c), Eq. (30) also leads to

$$\eta_\alpha^1 = 0 \quad \forall \alpha, \quad \alpha = 1, 2, \quad \forall x \in \Omega_\pm.$$
(31)

In other words, the leading order outer solution solves the outer problem exactly. Therefore, we have

$$u_\alpha^l = \eta_\alpha^l = 0 \quad \forall \alpha, \quad \alpha = 1, 2, \quad l > 0, \quad \forall x \in \Omega_\pm.$$
(32)

Let us now define a local orthogonal coordinate system (r, s), where r is the normal distance from the point x in Ω to the interface $\Gamma(t)$, such that $r > 0$ in Ω_+ and $r < 0$ in Ω_-, and $s = \{s_1, s_2\}$ being the other two coordinates that are perpendicular to r and tangent to Γ (see Fig. 1). Moreover, since the interface width is of order ε, we further introduce a stretched variable, $z = r/\varepsilon$. Therefore, (z, s) is a local orthogonal coordinate system that moves with the interface. In the moving coordinate system (MCS), the spatial and time derivatives transform as follows:

$$\nabla^2 = \varepsilon^{-2} \partial_z^2 + \varepsilon^{-1} \kappa\, \partial_z + \nabla_s^2,$$
(33a)

$$(\partial_t)_{\text{MCS}} = \partial_t + V \cdot \nabla \rightarrow \partial_t = (\partial_t)_{\text{MCS}} - \varepsilon^{-1} V^n \partial_z.$$
(33b)

In the above, ∇_s^2 is the 2D surface Laplacian, V^n is the normal velocity of the interface with respect to a stationary frame of reference, and κ is the curvature of the interface, which is positive when the center of curvature lies within Ω_-. We will drop the subscript (MCS) in the following.

In the inner region, we expand the fields as

$$\tilde{u}_\alpha(z, s, t) \equiv u_\alpha(r, s, t)$$
$$= \tilde{u}_\alpha^0(z, s, t) + \varepsilon\tilde{u}_\alpha^1(z, s, t) + \varepsilon^2\tilde{u}_\alpha^2(z, s, t) + \cdots$$
$$\forall \alpha, \quad \alpha = 1, 2,$$
(34)

with similar expressions for other field quantities. Again, similar to the outer expansion, we can get explicit expressions for these terms. Using Eqs. (26a, 33a, and 17b), we get

$$\tilde{u}_1^0 = \partial_{\tilde{\eta}_1} f(\tilde{\eta}_1^0, \tilde{\eta}_2^0) - \partial_z^2 \tilde{\eta}_1^0, \quad \tilde{u}_2^0 = \partial_{\tilde{\eta}_2} f(\tilde{\eta}_1^0, \tilde{\eta}_2^0) - \partial_z^2 \tilde{\eta}_2^0, \tag{35a}$$

$$\tilde{u}_1^1 = \partial_{\tilde{\eta}_1}^2 f(\tilde{\eta}_1^0, \tilde{\eta}_2^0) \tilde{\eta}_1^1 + \partial_{\tilde{\eta}_1 \tilde{\eta}_2}^2 f(\tilde{\eta}_1^0, \tilde{\eta}_2^0) \tilde{\eta}_2^1 - \kappa \partial_z \tilde{\eta}_1^0 - \partial_z^2 \tilde{\eta}_1^1, \tag{35b}$$

$$\tilde{u}_2^1 = \partial_{\tilde{\eta}_2}^2 f(\tilde{\eta}_1^0, \tilde{\eta}_2^0) \tilde{\eta}_2^1 + \partial_{\tilde{\eta}_2 \tilde{\eta}_1}^2 f(\tilde{\eta}_1^0, \tilde{\eta}_2^0) \tilde{\eta}_1^1 - \kappa \partial_z \tilde{\eta}_2^0 - \partial_z^2 \tilde{\eta}_2^1. \tag{35c}$$

Therefore, the inner equations can now be written as

$$\varepsilon^2 \partial_t \tilde{\eta}_\alpha - \varepsilon v \partial_z \tilde{\eta}_\alpha = -L \tilde{u}_\alpha \quad \forall \alpha, \; \alpha = 1, \; 2. \tag{36}$$

Here v is the interface (front) normal velocity in the slow timescale defined above. Again, the above inner equations must be solved simultaneously order by order. For the leading order (ε^0), we have

$$0 = -L \tilde{u}_\alpha^0 \quad \forall \alpha, \quad \alpha = 1, \; 2. \tag{37}$$

This gives

$$\tilde{u}_\alpha^0 = 0 \quad \forall \alpha, \quad \alpha = 1, \; 2. \tag{38}$$

These are basically the Euler–Lagrange equations (see Eq. 35a) which, with the boundary conditions, from the outer solution, e.g., $\tilde{\eta}_\alpha^0(\pm\infty) = \eta_\alpha^0(\pm 0)$, give the equilibrium planar profiles for the order parameters [6, 32]. For the next-to-the leading order (ε), we obtain

$$-v \partial_z \tilde{\eta}_\alpha^0 = -L \tilde{u}_\alpha^1 \quad \forall \alpha, \quad \alpha = 1, \; 2. \tag{39}$$

Following the standard procedure implemented in all previous asymptotic analyses [24, 35–40], we multiply each equation by its corresponding $\partial_z \tilde{\eta}_\alpha^0$ and integrate from $z \to -\infty$ to $z \to +\infty$. Performing integration by parts on the first and fourth terms of the right hand sides (see Eqs. 35b and 35c) and taking into account that the leading order profiles satisfy the Euler–Lagrange equations, one obtains

$$\frac{v\gamma_1}{\varepsilon} = L\left(A - \frac{\kappa\gamma_1}{\varepsilon}\right), \tag{40a}$$

$$\frac{v\gamma_2}{\varepsilon} = -L\left(A + \frac{\kappa\gamma_2}{\varepsilon}\right). \tag{40b}$$

In the above, $A(s,t) = \int_{-\infty}^{+\infty} (\tilde{\eta}_1^1 \partial_z \tilde{\eta}_2^0 - \tilde{\eta}_2^1 \partial_z \tilde{\eta}_1^0) \, \partial_{\tilde{\eta}_1 \tilde{\eta}_2}^2 f(\tilde{\eta}_1^0, \tilde{\eta}_2^0) \, \mathrm{d}z$, and $\gamma_\alpha = \int_{-\infty}^{+\infty} \varepsilon (\partial_z \tilde{\eta}_\alpha^0)^2 \mathrm{d}z$ such that the total grain boundary energy is $\gamma^{gb} = \gamma_1 + \gamma_2$. Hence, by eliminating A from the above two equations, we arrive at the desired result:

$$V^n = -L \varepsilon^2 \kappa. \tag{41}$$

Comparing this with its sharp-interface counterpart (Eq. 4), we get the relation

$$L\varepsilon^2 = \gamma^{gb} M_b. \tag{42}$$

Derivation of the equation of motion of a free (pore) surface

Consider a volume containing a free surface between the pore phase and a solid grain (see Fig. 1b), the free energy (Eq. 16) reduces to

$$F = \int \left[\mathrm{f}(\rho, \eta) + \frac{q\varepsilon^2}{2} |\nabla \rho|^2 + \frac{\varepsilon^2}{2} |\nabla \eta|^2 \right] \mathrm{d}^3 x. \tag{43}$$

The bulk free energy (Eq. 7) reduces to

$$f(\rho, \eta) = B\rho^2(1-\rho)^2 + C\left[\rho^2 + 6(1-\rho)\eta^2 - 4(2-\rho)\eta^3 + 3\eta^4\right]. \tag{44}$$

Hence, at a pore surface, the multi-well potential reduces to a double well potential reflecting the two equilibrium phases (see Fig. 1b). Noting that $L = \gamma^{gb} M_b \varepsilon^{-2}$ (from Eq. 42), the dynamical system (Eqs. 18 and 19) reduces to

$$\varepsilon^2 \partial_t \rho = \nabla \cdot M(\rho)\nabla\mu, \tag{45a}$$

$$\varepsilon^4 \partial_t \eta = -\gamma^{gb} M_b u \tag{45b}$$

with the following initial and boundary conditions (see Fig. 1b):

$$\eta(x,0) = 0, \quad \rho(x,0) = 0, \quad \forall x \in \Omega_-, \tag{46a}$$

$$\eta(x,0) = 1, \quad \rho(x,0) = 1, \quad \forall x \in \Omega_+, \tag{46b}$$

$$\mathbf{m} \cdot \nabla\eta = \mathbf{m} \cdot \nabla\rho = \mathbf{m} \cdot M\nabla\mu = 0, \quad \forall x \in \partial\Omega. \tag{46c}$$

Performing an outer expansion as before and substituting Eqs. (17a and 17b), we obtain

$$\mu^0 = \partial_\rho f(\rho^0, \eta^0), \quad u^0 = \partial_\eta f(\rho^0, \eta^0), \tag{47a}$$

$$\mu^1 = \partial_\rho^2 f(\rho^0, \eta^0) \rho^1 + \partial_{\rho\eta}^2 f(\rho^0, \eta^0) \eta^1,$$
$$u^1 = \partial_\eta^2 f(\rho^0, \eta^0) \eta^1 + \partial_{\eta\rho}^2 f(\rho^0, \eta^0) \rho^1. \tag{47b}$$

The outer equations can now be solved as follows. For the leading order (ε^0), we have

$$0 = \nabla \cdot M(\rho^0)\nabla\mu^0, \tag{48a}$$

$$0 = -\gamma^{gb} M_b u^0. \tag{48b}$$

When the initial and boundary conditions (Eqs. 46a–c) are taken into account, this gives

$$u^0 = \mu^0 = 0, \quad \forall x \in \Omega_\pm, \tag{49a}$$

$$\rho^0 = \eta^0 = 0, \quad \forall x \in \Omega_-, \tag{49b}$$

$$\rho^0 = \eta^0 = 1, \quad \forall x \in \Omega_+. \tag{49c}$$

For the next-to-the leading order (ε), we obtain

$$0 = \nabla \cdot M(\rho^0)\nabla\mu^1, \tag{50a}$$

$$0 = -\gamma^{gb}M_b u^1. \tag{50b}$$

Hence, we also deduce that

$$u^1 = \mu^1 = 0, \quad \forall x \in \Omega_{\pm}, \tag{51a}$$

$$\eta^1 = \rho^1 = 0, \quad \forall x \in \Omega_{\pm}. \tag{51b}$$

In the above, we deduced Eq. (51b) from (51a) using the same argument we utilized before in deriving Eq. (31) from (30). Therefore, once again the outer problem is solved exactly by the leading order outer solution and we have

$$u^l = \mu^l = \eta^l = \rho^l = 0, \quad l > 0, \quad \forall x \in \Omega_{\pm}. \tag{52}$$

In the vicinity of the free surface, we define an orthogonal coordinate system as before. The spatial and time derivatives are exactly as in Eq. (33). Additionally, here we have

$$\nabla \cdot (M\nabla\mu) = \varepsilon^{-2}\partial_z(\tilde{M}\partial_z\tilde{\mu}_\alpha) + \varepsilon^{-1}\tilde{M}\kappa\,\partial_z\tilde{\mu} + \nabla_s \cdot (\tilde{M}\nabla_s\tilde{\mu}), \tag{53}$$

where ∇_s, and ∇_s. are the 2D surface gradient and divergence, respectively. We then proceed by performing an inner expansion of the fields as before. We can then find explicit expressions for the different orders of $\tilde{\mu}$ and $\tilde{u}$ as follows:

$$\tilde{\mu}^0 = \partial_{\tilde{\rho}}f(\tilde{\rho}^0, \tilde{\eta}^0) - q\partial_z^2\tilde{\rho}^0, \quad \tilde{u}^0 = \partial_{\tilde{\eta}}f(\tilde{\rho}^0, \tilde{\eta}^0) - \partial_z^2\tilde{\eta}^0, \tag{54a}$$

$$\tilde{\mu}^1 = \partial_{\tilde{\rho}}^2 f(\tilde{\rho}^0, \tilde{\eta}^0)\,\tilde{\rho}^1 + \partial_{\tilde{\rho}\tilde{\eta}}^2 f(\tilde{\rho}^0, \tilde{\eta}^0)\,\tilde{\eta}^1 - q\kappa\,\partial_z\tilde{\rho}^0 - q\partial_z^2\tilde{\rho}^1, \tag{54b}$$

$$\tilde{u}^1 = \partial_{\tilde{\eta}}^2 f(\tilde{\rho}^0, \tilde{\eta}^0)\,\tilde{\eta}^1 + \partial_{\tilde{\eta}\tilde{\rho}}^2 f(\tilde{\rho}^0, \tilde{\eta}^0)\,\tilde{\rho}^1 - \kappa\,\partial_z\tilde{\eta}^0 - \partial_z^2\tilde{\eta}^1. \tag{54c}$$

Hence, the inner equations can now be written as

$$\varepsilon^4\partial_t\tilde{\rho} - \varepsilon^3 v\partial_z\tilde{\rho} = \partial_z(M(\tilde{\rho}^0)\partial_z\tilde{\mu}) + \varepsilon M(\tilde{\rho}^0)\kappa\,\partial_z\tilde{\mu} + \varepsilon^2\,\nabla_s \cdot (M(\tilde{\rho}^0)\nabla_s\tilde{\mu}), \tag{55a}$$

$$\varepsilon^4\partial_t\tilde{\eta} - \varepsilon^3 v\partial_z\tilde{\eta} = -\gamma^{gb}M_b\tilde{u}. \tag{55b}$$

These inner equations must be solved simultaneously. For the leading order (ε^0), we have

$$0 = \partial_z(M(\tilde{\rho}^0)\partial_z\tilde{\mu}^0), \tag{56a}$$

$$0 = -\gamma^{gb}M_b\tilde{u}^0. \tag{56b}$$

The above equations to be solved with boundary conditions that can be derived from the outer solutions via the matching conditions: $\partial_z\tilde{\mu}^0(\pm\infty) = 0$, $\tilde{\mu}^0(\pm\infty) = \mu^0(\pm0) = 0$, and $\tilde{u}^0(\pm\infty) = u^0(\pm0) = 0$; this gives

$$\tilde{u}^0 = \tilde{\mu}^0 = 0. \tag{57}$$

Therefore, once again, these are simply the Euler–Lagrange equations (see Eq. 54a). When these equations are supplemented with the boundary conditions from the outer solution, e.g., $\tilde{\rho}^0(\pm\infty) = \rho^0(\pm0)$ and $\tilde{\eta}^0(\pm\infty) = \eta^0(\pm0)$, they give the equilibrium planar profiles for the order parameters [6, 32]. For the next-to-the leading order (ε), we obtain (recall that $\tilde{\mu}^0 = 0$)

$$0 = \partial_z(M(\tilde{\rho}^0)\partial_z\tilde{\mu}^1), \tag{58a}$$

$$0 = -\gamma^{gb}M_b\tilde{u}^1. \tag{58b}$$

Taking into account the matching condition $\partial_z\tilde{\mu}^1(\pm\infty) = \partial_r\mu^0(\pm0) = 0$, this leads to

$$\tilde{\mu}^1 = e(s,t), \tag{59a}$$

$$\tilde{u}^1 = 0. \tag{59b}$$

Here $e(s,t)$ is a function that does not depend on z, which is to be determined. To accomplish that we follow the same procedure we conducted before, i.e., we multiply Eq. (59a) by $\partial_z\tilde{\rho}^0$ and Eq. (59b) by $\partial_z\tilde{\eta}^0$ and integrate in z from $-\infty$ to $+\infty$, we get

$$\tilde{\mu}^1 = A_1 - \frac{\kappa\gamma_\rho}{\varepsilon}, \tag{60a}$$

$$0 = A_1 + \frac{\kappa\gamma_\eta}{\varepsilon}. \tag{60b}$$

In the above, $A_1(s,t) = \int_{-\infty}^{+\infty}(\rho^1\partial_z\tilde{\eta}^0 - \tilde{\eta}^1\partial_z\tilde{\rho}^0)\,\partial_{\tilde{\rho}\tilde{\eta}}^2 f(\tilde{\rho}^0, \tilde{\eta}^0)\,dz$, $\gamma_\rho = \int_{-\infty}^{+\infty} q\varepsilon(\partial_z\tilde{\rho}^0)^2 dz$, and $\gamma_\eta = \int_{-\infty}^{+\infty}\varepsilon(\partial_z\tilde{\eta}^0)^2 dz$ such that the total surface energy is given as $\gamma^s = \gamma_\rho + \gamma_\eta$. From the above two equations, one obtains

$$\tilde{\mu}^1 = \frac{-\kappa\gamma^s}{\varepsilon}. \tag{61}$$

For the next order (ε^2), we have (where the fact that $\tilde{\mu}^0 = \partial_z\tilde{\mu}^1 = 0$ was taken into account)

$$0 = \partial_z(M(\tilde{\rho}^0)\partial_z\tilde{\mu}^2), \tag{62a}$$

$$0 = -\gamma^{gb}M_b\tilde{u}^2. \tag{62b}$$

In conjunction with the matching condition $\partial_z\tilde{\mu}^2(\pm\infty) = \partial_r\mu^1(\pm0) = 0$, we arrive at

$$\tilde{u}^2 = \partial_z\tilde{\mu}^2 = 0. \tag{63}$$

The front velocity can be obtained at order (ε^3). At this level, it suffices to consider only Eq. (55a) which gives (recall that $\partial_z\tilde{\mu}^2 = 0$)

$$-v\,\partial_z\tilde{\rho}^0 = \nabla_s \cdot (\tilde{M}\nabla_s\tilde{\mu}^1) = \frac{-\gamma^s}{\varepsilon}M(\tilde{\rho}^0)\nabla_s^2\kappa \tag{64}$$

In Eq. (64) above, we have used the fact that $\tilde{\rho}^0$ does not depend on s. Multiplying Eq. (64) by $\partial_z \tilde{\rho}^0$ and integrating in z from $-\infty$ to $+\infty$ produces

$$v \frac{\gamma_\rho}{q\varepsilon} = \frac{\gamma^s \bar{M}^s}{\varepsilon} \nabla_s^2 \kappa, \tag{65}$$

where $\bar{M}^s = \int\limits_{-\infty}^{+\infty} M(\tilde{\rho}^0) \partial_z \tilde{\rho}^0 dz = \int\limits_0^1 M(\rho^0) d\rho^0$.

Note that $\bar{M}^s$ is finite whether $M \to 0$ for $z \to \pm\infty$ or simply a constant. Hence, in agreement with [35], we show that as far as the asymptotic analysis is concerned, the Cahn–Hilliard equation recovers surface motion by surface diffusion regardless of the form of the mobility as long as the outer solutions for the order parameters represent the equilibrium bulk phases. Nonetheless, using interpolation functions and projection tensors as in Eq. (13) to represent surface diffusion in phase field models is important from numerical point of view. Recall that we conclude that the normal gradient of the chemical potential is zero in the interfacial region ($\partial_z \tilde{\mu} = 0$) using matching conditions that assume $\varepsilon \to 0$. However, in any numerical implementation the diffuse-interface width is finite, and hence, non-zero normal fluxes may exist in the interfacial region during simulations. The projection tensor ensures that the normal fluxes in the interfacial region vanish even if the normal gradients of the chemical potential are non-zero. On the other hand, the interpolation function ensures the bulk fluxes vanish even if the numerical values of the order parameters differ slightly from their equilibrium values due to any numerical errors. However, this is usually negligible, and hence, using interpolation functions is often unnecessary. Finally, restoring the physical unit of the velocity, Eq. (65) becomes

$$V^n = (1 + q)\bar{M}^s \varepsilon^2 \nabla_s^2 \kappa. \tag{66}$$

In obtaining Eq. (66), we used the relation $q = \gamma_\rho/\gamma_\eta$, and hence $\gamma^s/\gamma_\rho = (1 + q)/q$ which arises from the similar behavior of the equilibrium profiles a cross a free surface (see Ref. [6] for details). By comparing Eq. (66) with its sharp-interface counterpart, Eq. (5), we obtain the relation

$$(1 + q)\bar{M}^s \varepsilon^2 = \frac{\gamma^s D_s w \, v_m}{RT}. \tag{67}$$

So far, we have shown that the equations of motions for the free (pore) surface and the grain boundary in the phase field model reduce to their counterparts in sharp-interface model. However, in order to prove that the phase field model completely recovers the sharp-interface model, the boundary conditions at the triple-junction, namely, the balance of forces, fluxes, and continuity of chemical potential must be derived. Such derivation was presented in the phase field models [39, 40] which have the same structure as the one presented here as we mentioned in the beginning of this section. Their derivation is readily applicable to our model, and hence, we will not repeat it here

Results and discussion

A standard explicit finite difference numerical scheme has been used to solve the kinetic Eqs. (12 and 15) in 3D. In this scheme, a second-order-centered finite difference approximation was utilized for all spatial derivatives and an explicit Euler scheme was used to discretize the time derivatives. A Voronoi tessellation was utilized to generate the initial polycrystalline structure, and each grain was assigned a different order parameter to avoid artificial coalescence of grains during the simulation. In most of the simulations presented here, pores were distributed randomly on grain boundaries to mimic the actual microstructure of the material. However, the number and distribution of pores were varied to investigate their effect on the kinetics of grain growth. In all simulations presented here, an ensemble of 100 grains (and hence 100 non-conserved order parameters) on a $(192)^3$ finite difference grid was used. Periodic boundary conditions were applied in the three directions. Parallel computing was used to overcome the high computational demand of the problem. Each simulation run was conducted on a single node with 48 cores using the shared-memory parallelization concept. The typical computing time for each simulation ranged from 1 week to 1 month depending on the porosity level. We stopped the simulations when only one quarter of the initial number of grains (25 grains) remained for the sake of good statistics.

In applying our model to CeO_2, surface and grain boundary energies of ceria were taken to be 1.5 and 1.0 J/m^2, respectively [41], and orientation dependence of these energies was ignored for simplicity. The surface diffusivity of CeO_2 is given by [41]

$$D^s = 3.82 \times 10^{-4} \exp\left(\frac{-308250}{RT}\right) \text{ m}^2/\text{s} . \tag{68}$$

The intrinsic grain boundary mobility was obtained from the experimental data by Chen and Chen [42]. Their data were chosen because their samples were pure and almost fully dense. They have deduced a value of the activation energy of 581 kJ/mole for the grain growth process. However, they did not provide a formula for the grain boundary mobility. Here, we fit their data to the expression:

$$M_b = 327.1 \, \exp\left(\frac{-581000}{RT}\right) \text{ m}^4/\text{J s} . \tag{69}$$

With the above materials parameters at hand, all phase field parameters can be fixed using Eqs. (8–11, 42, 67). Physically, the diffuse-interface width is on the order of few surface layers or the grain boundary thickness. However, this gives rise to a computational difficulty; since a few mesh points must lie within the diffuse interface, and thus, the grid size must be a fraction of nanometer, which

Fig. 2 Snapshots of the 3D microstructure during grain growth in fully dense (pore-free) ceria at 1700 K: **a** at 1 min, **b** at 60 min, and **c** at 180 min. As large grains grow at the expense of smaller grains, the number of grains decreases and the average grain size increases with time
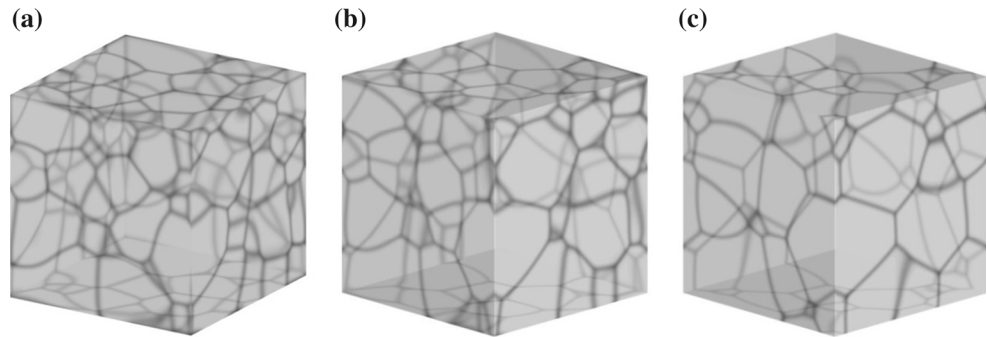

Fig. 3 Kinetics of grain growth in fully dense (pore-free) CeO_2. **a** Growth kinetics follows the parabolic growth law given by Eq. (69) with $k = 3.34$ μm^2/h at 1700 K, $k = 29.07$ μm^2/h at 1800 K, and $k = 279.8$ μm^2/h at 1900 K. **b** An Arrhenius plot for the rate constant showing activation energy of 576.8 kJ/mole which is in good agreement with the value of 581 kJ/mole reported from experiments [42]. The *markers* represent the data from simulations, and the lines are the best fit
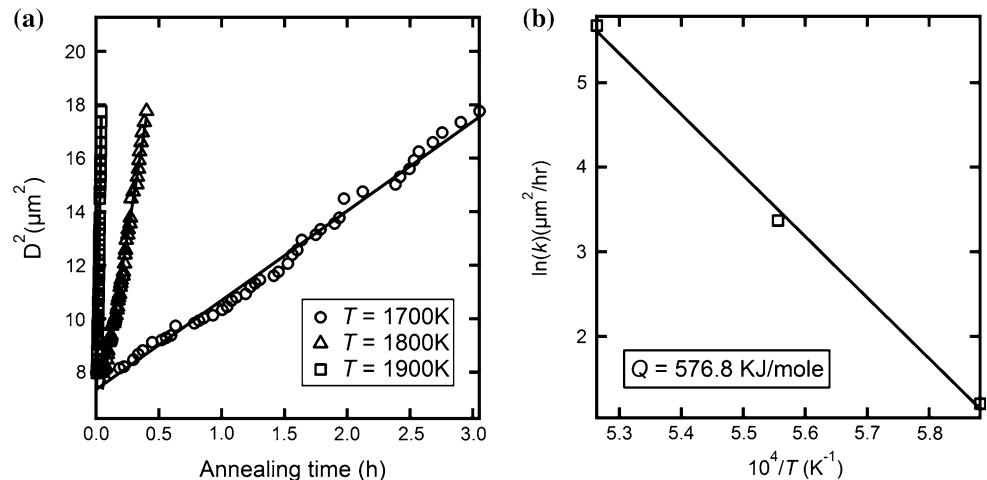
renders mesoscale simulations unfeasible. Nevertheless, as can be seen from the formalism above, one may increase the diffuse-interface width without altering the thermodynamic forces or the kinetics in the system. This can be accomplished by considering a computationally convenient diffuse-interface width and calculating the model parameters accordingly [6, 18]. Here we use a diffuse-interface width of 0.2 μm and a grid size of 0.067 μm.

First, we investigate the grain growth in pure, fully dense ceria. In such a system, the grain growth kinetics is expected to follow the well-known parabolic growth [7, 8], which has the form

$$D^2(t) - D_0^2 = k t. \tag{70}$$

Here k is the rate constant of the growth process, and it is related to the grain boundary mobility by $k = 2\gamma^{gb}M_b$ [1, 18]. For ceria, such ideal grain growth was also reported from experiments by Chen and Chen [42]. Our model results are presented in Figs. 2 and 3 below. Figure 2 shows snapshots of the microstructure evolution of ceria at 1700 K. The microstructure is visualized by plotting the function $\phi(x,t) = \sum_{\alpha=1}^{100} \eta_\alpha^2(x,t)$, which takes on the value of 0 in the pore phase and 1 in each grain of the solid phase, and it varies smoothly across the grain boundaries and the

free (pore) surface. As it is evident from Fig. 2, large grains grow at the expense of smaller ones, and hence, the average grain size increases with time. This is quantitatively described in Fig. 3. Figure 3a demonstrates that the growth follows the parabolic law given by Eq. (70). The average grain size at time t, $D(t)$, is approximated by $D(t) = \Omega_g^{1/3}(t)$, where $\Omega_g(t)$ is the average grain volume at time t. The average grain volume is directly calculated as $\Omega_g(t) = \sum_{\alpha=1}^{100} \int_\Omega \eta_\alpha / N_g(t)$, with $N_g(t)$ being the total number of grains at time t. The effect of the temperature on the grain growth simulations was considered through the dependence of the boundary mobility on the temperature as given by Eq. (69). As it is clear from Fig. 3a, the growth enhances as the temperature increases. The rate constant has the value $k = 3.34$ μm^2/h at 1700 K, $k = 29.07$ μm^2/h at 1800 K, and $k = 279.8$ μm^2/h at 1900 K. Using these values of the rate constant at different temperatures, an Arrhenius plot of the process can be generated. This is shown in Fig. 3b, where the activation energy was found to be 576.8 kJ/mole, which is in good agreement with the expected value of 581 kJ/mole from Eq. (69).

Now we turn our attention to the case of grain growth in porous ceria. As we discussed before, pores exert a drag
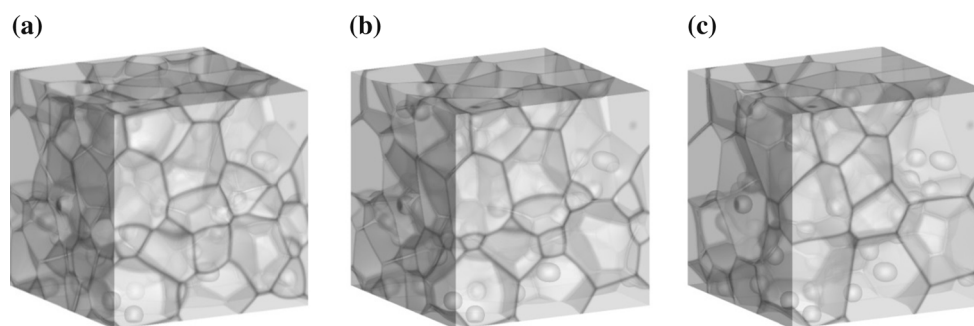
(a)   **(b)**   **(c)**

Fig. 4 Snapshots of the 3D microstructure evolution in porous ceria at 1700 K: **a** after 1 min, **b** at 120 min, and **c** at 360 min. Pore breakaway is evident. Some pores break away from the grain boundaries and some move along with them. The grains that left pores behind are relatively larger than the neighboring ones; this implies that pore breakaway initiates abnormal grain growth

force on the boundary that hinders its motion and hence retard the grain growth process. However, as expected from grain growth theories and reported from experiments, there are several pore-boundary interactions that may occur. A pore may separate from the boundary or move along with it. Moreover, an isolated pore inside a grain may get picked up by a migrating boundary. Furthermore, when a pore moves along with the boundary, the kinetics of the pore-boundary complex may be pore controlled or boundary controlled. Therefore, a good model should be able to elucidate all these possibilities. Here we demonstrate that the phase field model is indeed capable of capturing all such scenarios.

Snapshots of the microstructure evolution in porous ceria at 1700 K are shown in Figs. 4 and 5 below. In this simulation, an ensemble of 100 grains with initial average grain size of 2.5 μm and 80 spherical pores with initial pore size of 0.8 μm was used. Half of the pores were distributed randomly on the grain boundary network and the rest were distributed randomly inside the grains to capture all possible pore-boundary interactions. The initially spherical pores relax quickly to a shape that satisfies locally the equilibrium dihedral angle condition at triple-junctions. Figure 4 presents snapshots of the 3D microstructure evolution. Figure 5 shows different 2D cross-sectional views of the same 3D simulation. As it is evident from the figures, there is a continuous change of the pore and boundary shapes during the migration of the pore-boundary complex. Moreover, the pore breakaway phenomenon is clearly captured. In our previous 2D simulations, the pore breakaway phenomenon was artificially suppressed due to the unrealistic cylindrical symmetry of the pores and grains implicitly assumed in 2D simulations. Such situation was also reported in the sharp-interface simulations [14–17]. Also in agreement with the sharp-interface predictions, the phase field model demonstrates that the pore breakaway possibility depends strongly on the pore configuration. Pores on two-grain boundary (edge pores) can easily separate from a migrating boundary, while higher-order

configurations, e.g., pores on three- and four-grain junctions, tend to move along with the boundary. These situations are particularly clear in Fig. 5. Nonetheless, the higher-order pore configurations can reduce to lower-order configuration when one or more of the grain boundaries separate from the pore; this can be considered as a partial breakaway. The opposite scenario is also possible, i.e., migrating boundaries can attach themselves to a lower-order configuration and form a higher-order configuration; this can also be considered as a partial attachment. Moreover, a pore that started as an isolated pore inside a grain could get picked up by a migrating boundary and then separate from it and then get picked up by another boundary and so on. Similar situation with opposite order could occur for isolated pores on grain boundaries. In another words, a specific pore could go through a series of partial and complete attachments and separations. Lastly, as can be deduced from Figs. 4 and 5, most of the grains where pore separation took place are larger than their neighboring grains. This demonstrates that pore breakaway initiates abnormal grain growth as predicted from grain growth theories and reported in experiments [1, 11–18].

Since the 3D simulations with the current model are clearly able to account for all the possible pore-boundary interactions, it is now possible to investigate quantitatively the effects of the presence of pores on the grain growth in ceria. In doing so, we use different ensembles of grains and pores. Initially, the pores are spherical and randomly distributed on grain boundaries to mimic actual microstructures during the final stage of sintering. The initial average grain size was 2.5 μm and the pore size was 0.8 μm. The number of pores (and hence their volume fraction, f) was varied to study its effect on the kinetics of grain growth.

In agreement with our previous 2D simulations [6, 18], the presence of pores diminishes grain growth in porous ceria. This effect is quantitatively captured in Fig. 6, which shows the evolution of the average grain size with different levels of porosity at 1700 K. As it is obvious from the figure, the grain growth process slows down as the amount
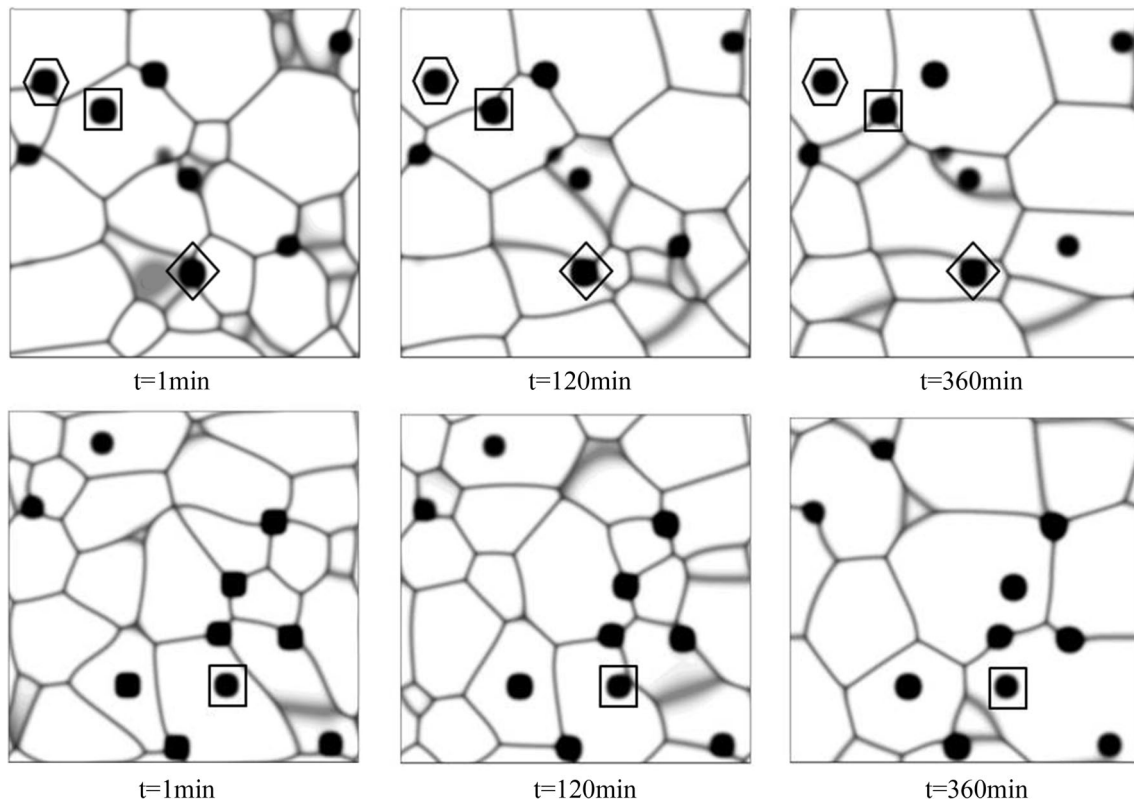
t=1min   t=120min   t=360min

t=1min   t=120min   t=360min

Fig. 5 Snapshots of cross-sectional views corresponding to the results shown in Fig. 4 revealing pore-boundary interactions: x–z plane (*upper row*) and y–z plane (*lower row*). The change of the pore shape is continuous during the movement of a pore-boundary complex. A pore can break away from or be picked up by a migrating grain boundary (e.g., the pores in *hexagon* and *square*, respectively, in the *upper row*). The pore breakaway possibility is highly dependent on the pore configuration. Higher-order pore configurations (e.g., the pores at three- and four-grain junctions) tend to reduce to the two-grain junction (*edge pore*) configuration, which represents a partial breakaway (e.g., the pore marked by *diamonds* in the *upper row*) before complete separation. A pore on a two-grain junction could also become attached to other migrating boundaries and form a higher-order configuration (e.g., the pore enclosed in *squares* in the *upper row*). A specific pore could go through a series of attachments and detachments (e.g., the pore marked by the *rectangle* in the *lower row*). The *thick gray spots* are due to the fact that the cutting planes are sometimes parallel to the diffuse interfaces
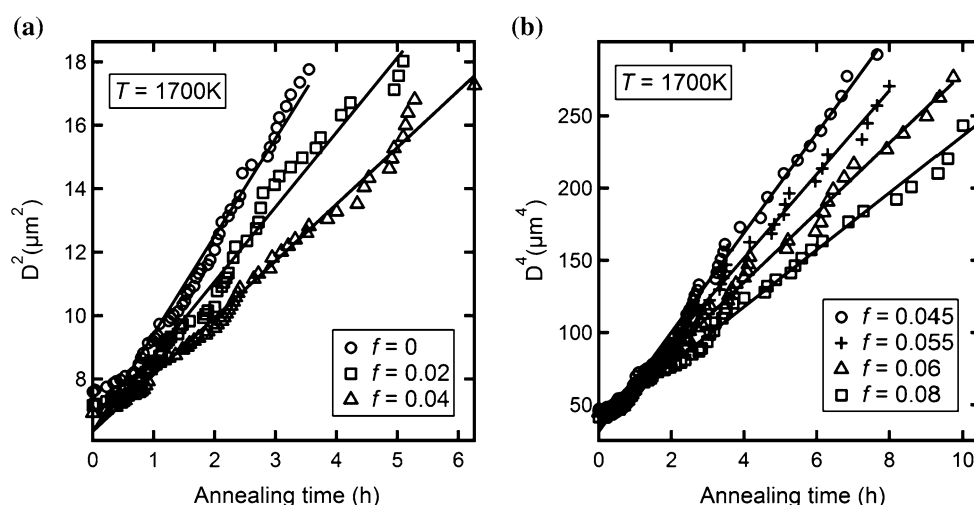
Fig. 6 Effect of porosity on the kinetics of grain growth in CeO$_2$ at 1700 K. **a** Evolution of the average grain size with time as function of the pore volume fraction. The main trend is the same as was captured in 2D simulations [6, 18]. That is, the process of grain growth is slowed down by increasing the amount of porosity. **b** A close-up view showing the initial dense region in part (**a**)
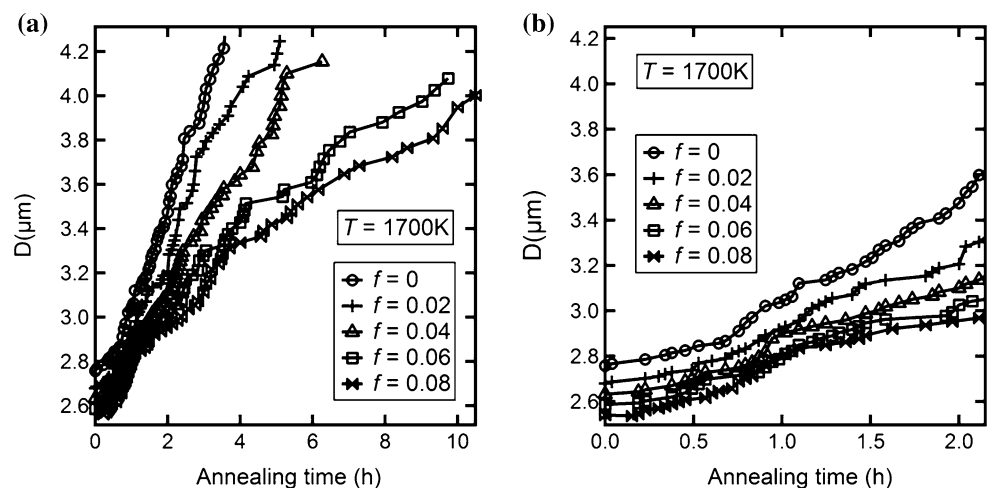
of porosity increases. Moreover, the average kinetics of the heterogeneous system shows a transition from boundary-controlled kinetics to pore-controlled kinetics as the porosity level increases. Such situation is presented in Fig. 7. This prediction agrees with both the classical models [11–13] and the sharp-interface models [16, 17].

However, the phase field model presented here relaxes all the assumptions used in those models. For example, it does not assume a homogeneous microstructure as in the classical models [1, 11–13]. It is also not restricted to simplified geometrical descriptions of the pore/boundary configurations or steady-state situations as in the sharp-interface models [14–17]. The condition that determines which kinetics dominates is as follows. In terms of the phase field parameters, when $\bar{M}^s\kappa_\rho \ll f\,r^2 L\kappa_\eta$, the system follows pore-controlled kinetics, while in the case $\bar{M}^s\kappa_\rho \gg f\,r^2 L\kappa_\eta$, it follows boundary-controlled kinetics. Here r is the pore size. Equivalently, in terms of the regular thermodynamic and kinetic (sharp-interface) parameters, this condition becomes as follows: if $\frac{\gamma^s D_s w v_m}{RT} \ll f\,r^2 M_b \gamma^{gb}$, the growth kinetics is pore-controlled, while if $\frac{\gamma^s D_s w v_m}{RT} \gg f\,r^2 M_b \gamma^{gb}$, the growth kinetics is boundary-controlled. This criterion can easily be understood if one recalls the equation of motions for the grain boundary and pore (free) surface in the diffuse- or sharp-interface descriptions (Eqs. 41 and 67 or 4 and 5). Aside from the pore fraction, this condition simply examines if the grain boundary velocity is higher or lower than the pore (free) surface velocity. The pore fraction simply checks if the porosity is of significant amount to influence the average kinetics of the system. It is also worth noting that the rate constant (or equivalently the activation energy) is sensitive to the precise amount of porosity regardless of the type of the prevailing kinetics. This is also shown in Fig. 7 where the slope (rate constant) decreases with increasing the porosity level for both boundary- and pore-controlled kinetics. The quantitative results are summarized in Tables 1 and 2, which give the values of the rate constant as function of the pore fraction for both the types of kinetics.

The system may exhibit mixed kinetics if the above condition for the two limiting cases does not hold. Such

Table 1 The dependence of the rate constant on the pore fraction for boundary-controlled kinetics

f (%)	k (μm^2/h)
0	3.34
2	2.35
4	1.79

Table 2 The dependence of the rate constant on the pore fraction for pore-controlled kinetics

f (%)	k (μm^4/h)
4.5	34.4
5.5	28.94
6	24.1
8	19.73

type of kinetics, as was shown in our previous 2D simulations [6, 18], is identified with an intermediate value for the growth exponent between two and four. However, this intermediate region may be narrow or wide depending on the pore configuration. In the results of Figs. 6 and 7, the transition from boundary-controlled kinetics to pore-controlled kinetics occurred sharply at 4 % porosity level. Nonetheless, when we used different initial configurations with more higher-order pore configurations, an intermediate region appeared. This is shown in Fig. 8 where two different initial configurations with different number of higher-order pore configurations were used. In configuration II, 65 % of the pores were of higher-order configurations and the rest were edge pores. In configuration III, 80 % of the pores were of higher-order configurations. As shown in Fig. 8, at porosity level of 4 %, both configurations exhibited mixed kinetics with growth exponent of 3. However, the rate constant was lower for the initial configuration with more higher-order pore configurations. This is consistent with the fact that higher-order pore configurations cannot easily detach from the grain boundary as
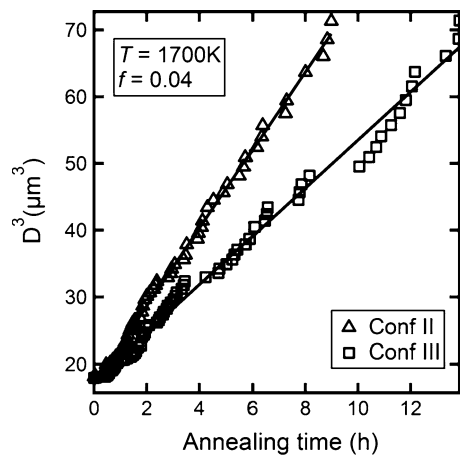
Fig. 8 Mixed-kinetics grain growth of 4 % porous ceria at 1700 K. Initial configurations II and III have more pores on triple and quadruple junctions than the initial configuration corresponding to the results in Figs. 6 and 7. These configurations exhibit mixed-kinetics growth between 4 and 6 % porosity levels. Moreover, the rate constant (the slope) increases as the initial amount of the higher-order pore configurations increases. This strong dependence of the overall kinetics on the initial configuration is due to the fact that the pore breakaway possibility is highly dependent on the pore configurations. Higher-order pores do not separate from a migrating boundary, while edge pores (pores on two-grain junctions) easily detach from a migrating boundary

we discussed before. The intermediate region in both configurations was between 4–6 % porosity with boundary-controlled kinetics below 4 % and pore-controlled kinetics above 6 %.

The strong dependence of the overall grain growth kinetics on the precise amount and distribution of pores captured by the phase field model explains the discrepancies often found in the results obtained from grain growth experiments in porous solids. For example, for the case of grain growth in ceria, different types of kinetics were reported. Chen and Chen [42] reported parabolic grain growth kinetics for highly dense ceria samples. Our model results for the pore-free case are in good agreement with their data as we shown in the beginning of this section. Zhang and co-workers reported different kinetics for 2–8 % porous ceria [43–45]. For pure ceria, they reported a growth exponent of three with activation energies in the range 697–731 kJ/mole. This similar to the mixed-kinetics case we presented here (Fig. 8). The difference in the activation energy can be attributed to its sensitivity to the precise amount and distribution of pores as we discussed above. They also reported a growth exponent of four for Co-, Mn-, and Fe-doped porous ceria with activation energies in the range 572–593 kJ/mole. This is similar to our results for the pore-controlled kinetics shown in Fig. 7b. Adding dopants is equivalent to changing the porosity level since it alters the intrinsic grain boundary mobility. In this

case, as reported by Zhang and co-workers [43–45], the dopants increased the intrinsic grain boundary mobility and hence shifted the kinetics from mixed kinetics to pore-controlled kinetics. However, the difference in the activation energies in this case is attributed to the presence of both pores and dopants. Therefore, the model results agree well with grain growth experiments in ceria.

Concluding remarks

An elaborate phase field study of grain growth in porous solids was conducted. The phase field model couples surface and grain boundary motion using a dynamical system of coupled Cahn–Hilliard and Allen–Cahn equations. Hence, it takes into account the interplay between the pore and the grain boundary which highly influences the overall grain growth kinetics. We carried out a formal asymptotic analysis to verify that the phase field model is consistent with the well-known sharp-interface description of the problem. The phase field model alleviates all the unrealistic assumptions of the classical homogeneous models and obviates all the numerical difficulties of the sharp-interface models. To the best of our knowledge, the 3D simulations presented here are the first such general simulations for 3D grain growth in porous solids in the literature.

The 3D phase field simulations capture all the physical aspects of grain growth in porous solids predicted from classical and sharp-interface models and observed in experiments. The 3D simulations demonstrated that the pore configuration is a key factor for the pore breakaway phenomenon. Higher-order pores (e.g., pores on three- and four-grain junctions) never separate directly from a migrating boundary, while pores on two-grain junctions (edge pores) can easily detach from a migrating boundary. However, higher-order pore configurations can transform to lower-order configurations and vice versa via the so-called partial breakaway and attachment phenomena. Hence, the pore distribution is an important factor in determining the overall grain growth kinetics. The pore fraction is another crucial factor in determining prevailing growth kinetics. The kinetics of grain growth in porous solids changes from boundary-controlled to pore-controlled as the amount of porosity increases. An intermediate region with mixed kinetics is also possible. The width of such an intermediate region depends on the initial pore distribution. In all these different growth regimes, the rate constant (or equivalently the activation energy) is sensitive to the precise amount and distribution of porosity. Therefore, a detailed description of the microstructure (e.g., pore fraction and pore and grain sizes and distributions) is necessary for obtaining accurate grain growth rates. While only grain growth in ceria was considered here, the basic trends of the

results are general and valid for all porous solids. The strong dependence of the grain growth kinetics on the underlying microstructure in porous solids captured by the phase field model helps in reconciling the discrepancies found in the experimental results for such materials.

In our investigation, we considered surface diffusion to be the sole mechanism for pore migration. However, for a complete description of the problem, bulk diffusion and evaporation and condensation must be incorporated as possible mechanisms for pore migration. It can be shown that only minor modifications are required for the current version of the model to account for these mechanisms. This will be the subject of an upcoming publication.

In all the simulations presented here, isotropic material properties, e.g., surface and grain boundary energies and mobilities, were assumed. For a more accurate description of grain growth in real materials, the anisotropy of these parameters must be taken into account. Such anisotropy is known to cause abnormal grain growth in fully dense solids. For the case of porous materials, it will certainly also affect the possibility of pore breakaway and hence the overall growth kinetics. The current version of the phase field model can be generalized to take into consideration the anisotropy of these parameters by allowing the gradient coefficients, Cahn–Hilliard mobility, and Allen–Cahn mobility to depend on the corresponding order parameters and/or their gradients. A detailed procedure for constructing such anisotropic phase field models was reported several times in the literature [24, 29].

References

1. Rahaman MN (2003) Ceramic processing and sintering, 2nd edn. Marcel Dekker, New York
2. Kingery WD, Bowen HK, Uhlmann DR (1976) Introduction to ceramics, 2nd edn. Wiley, New York
3. Turnbull JA (1974) The effect of grain size on the swelling and gas release properties of UO$_2$ during irradiation. J Nucl Mater 50:62
4. Olander DR (1976) Fundamental aspects of nuclear reactor fuel element. TID-26711-P1. Technical Information Service, Springfield
5. Was GS (2007) Fundamentals of radiation materials science-metals and alloys. Springer, Berlin
6. Ahmed K, Yablinsky CA, Schulte A et al (2013) Phase field modeling of the effect of porosity on grain growth kinetics in polycrystalline ceramics. Model Simul Mater Sci Eng 21:065005
7. Burke JE, Turnbull D (1952) Recrystallization and grain growth. Prog Metal Phys 3:220

8. Mullins W (1956) Two-dimensional motion of idealized grain boundaries. J Appl Phys 27:900
9. Hillert M (1965) On the theory of normal and abnormal grain growth. Acta Metall 13:227
10. Taylor JE, Cahn JW (1994) Linking anisotropic sharp and diffuse surface motion laws via gradient flows. J Stat Phys 77:183–197
11. Nichols FA (1968) Further comments on the theory of grain growth in porous compacts. J Am Ceram Soc 51:468
12. Brook RJ (1969) Pore-grain boundary interactions and grain growth. J Am Ceram Soc 52:56
13. Carpay FMA (1977) Discontinuous grain growth and pore drag. J Am Ceram Soc 60:82
14. Hsueh CH, Evans AG, Coble RL (1982) Microstructure development during final/intermediate stage sintering—I. Pore/grain boundary separation. Acta Metall 30:1269
15. Spears MA, Evans AG (1982) Microstructure development during final/intermediate stage sintering—II. Grain and pore coarsening. Acta Metall 30:1281
16. Svoboda J, Riedel H (1992) Pore-boundary interactions and evolution equations for the porosity and the grain size during sintering. Acta Metall Mater 40:2829
17. Riedel H, Svoboda J (1993) A theoretical study of grain growth in porous solids during sintering. Acta Metall Mater 41:1929
18. Ahmed K, Pakarinen J, Allen T, El-Azab A (2014) Phase field simulation of grain growth in porous uranium dioxide. J Nucl Mater 446:90
19. Barrett JW, Garcke H, Nurnberg R (2010) Finite-element approximation of coupled surface and grain boundary motion with applications to thermal grooving and sintering. Eur J Appl Math 21:519
20. Hayun S, Shavareva TY, Navrotsky A (2011) Nanoceria—energetics of surfaces, interfaces and water adsorption. J Am Ceram Soc 94:3992
21. Mihalache V, Pasuk I (2011) Grain growth, microstructure and surface modification of textured CeO$_2$ thin films on Ni substrate. Acta Mater 59:4875
22. Mullins W (1956) Theory of thermal grooving. J Appl Phys 28:333
23. Emmerich H (2008) Advances of and by phase-field modelling in condensed-matter physics. Adv Phys 57:1
24. Provatas N, Elder K (2010) Phase-field methods in materials science and engineering. Wiley, Weinheim
25. El-Azab A, Ahmed K, Rokkam S, Hochrainer T (2014) Diffuse interface modeling of void growth in irradiated materials. Mathematical, thermodynamic and atomistic perspectives. Curr Opin Solid State Mater Sci 18:90–98
26. Fan D, Chen LQ, Chen SP (1998) Numerical simulation of zener pinning with growing second-phase particles. J Am Ceram Soc 81:526
27. Wang Y (2006) Computer modeling and simulation of solid-state sintering: a phase field approach. Acta Mater 54:953
28. Chen LQ, Yang W (1994) Computer simulation of the domain dynamics of a quenched system with a large number of non-conserved order parameters: the grain-growth kinetics. Phys Rev B 50:15752
29. Moelans N, Blanpain B, Wollants P (2008) Quantitative analysis of grain boundary properties in a generalized phase field model for grain growth in anisotropic systems. Phys Rev B 78:024113
30. Kim SG, Park YB (2008) Grain boundary segregation, solute drag and abnormal grain growth. Acta Mater 56:3739
31. Cahn JW, Novic-Cohen A (2000) Motion by curvature and impurity drag: resolution of a mobility paradox. Acta Mater 48:3425
32. Cahn JW, Hilliard JE (1958) Free energy of a nonuniform system. I. Interfacial free energy. J Chem Phys 28:258
33. De Groot SR, Mazur P (1962) Non-equilibrium thermodynamics. North-Holland Publishing Company, Amesterdam

34. Cahn JW (1961) On spinodal decomposition. Acta Metall 9:795

35. Gugenberger C, Spatschek R, Kassner K (2008) Comparison of phase-field models for surface diffusion. Phys Rev E 78:016703

36. Allen SM, Cahn JW (1979) A microscopic theory for antiphase boundary motion and its application to antiphase domain coarsening. Acta Metall 27:1085

37. Fife PC (1992) Dynamics of internal layers and diffuse interfaces. SIAM, Philadelphia

38. Pego RL (1989) Front migration in the nonlinear Cahn–Hilliard equation. Proc Roy Soc London Ser A 422:261

39. Novic-Cohen A (2000) Triple-junction motion for an Allen–Cahn/Cahn–Hilliard system. Phys D 137:1

40. Barrett JW, Garcke H, Nurnberg R (2007) A phase field model for the electromigration of intergranular voids. Interfaces Free Bound 9:171–210

41. Zouvelou N, Mantzouris X, Nikolopoulos P (2008) Surface and grain-boundary energies as well as surface mass transport in polycrystalline CeO$_2$. Mat Sci Eng A 495:54

42. Chen P, Chen I (1996) Grain growth in CeO$_2$: dopant effects, defect mechanism, and solute drag. J Am Ceram Soc 79:1793

43. Zhang TS, Hing P, Huang H, Kilner J (2002) Sintering and grain growth of CoO-doped CeO$_2$ ceramics. J Eur Ceram Soc 22:27

44. Zhang TS, Hing P, Huang H, Kilner J (2002) Sintering study on commercial CeO$_2$ powder with small amount of MnO$_2$ doping. Mater Lett 57:507

45. Zhang TS, Ma J, Kong LB, Zeng ZQ, Hing P, Kilner J (2003) Final-stage sintering behavior of Fe-doped CeO$_2$. Mat Sci Eng B 103:177